

Reflection-mode diffraction tomography of multiple-scattering samples on a reflective substrate from intensity images

TONGYU LI,¹ JIABEI ZHU,¹ YI SHEN,¹ AND LEI TIAN^{1,2,*}

¹*Department of Electrical and Computer Engineering, Boston University, Boston, Massachusetts 02215, USA*

²*Department of Biomedical Engineering, Boston University, Boston, Massachusetts 02215, USA*

*leitian@bu.edu

Abstract: Strong substrate reflections and complex scattering effects present significant challenges for diffraction tomography in metrology and inspection applications. To address these issues, we introduce a reflection-mode diffraction tomography technique for imaging strongly scattering samples on a reflective substrate using intensity-only measurements. Our technique leverages the modified Born series to model complex wave interactions with fast and stable convergence, further incorporating Bloch and perfect electric conductor boundary conditions for improved accuracy. The adjoint method is used for efficient gradient computation in solving the inverse problem. Validated on a reflection-mode LED array microscope, we achieve high-resolution reconstructions of dual-layer targets and phase structures through a scattering fiber layer, demonstrating the technique’s potential for challenging metrology and inspection tasks.

1. Introduction

Diffraction tomography (DT) is a well-established, label-free, and non-destructive technique that enables the characterization of 3D refractive index (RI) distributions of samples. Traditionally, DT has been widely used in biomedical imaging [5] for monitoring cellular dynamics [3] and analyzing tissue morphology [4] using transmission-mode measurements, where light passes through the sample before detection. Recently, the scope of DT has expanded beyond biological applications, as it is increasingly explored for industrial metrology and inspection [14, 16, 19]. When applied to scenarios involving strongly reflective substrates, such as semiconductor wafers or metallic surfaces, DT requires adapting to reflection-mode measurements. In these cases, light is reflected by the substrate after passing through the sample, introducing new complexities that necessitate novel strategies for accurate reconstruction.

As the use of DT grows in semiconductor technology, the increasingly complex 3D architectures used in advanced devices present substantial challenges. These architectures, essential for enhancing device performance, are difficult to characterize accurately using traditional methods. Ensuring accurate measurements is crucial not only for optimizing production yields but also for accelerating research and development (R&D) cycles.

A primary challenge arises from the strong scattering processes that occur due to high RI contrasts between the structures of interest and the surrounding materials. Combined with the complexity of the 3D architectures, these RI differences result in intricate light propagation phenomena [31, 32] such as multiple scattering, cross-polarization and shadowing effects. These behaviors are not adequately modeled by traditional methods used in transmission-mode DT techniques, which typically rely on single-scattering [6, 21] or multi-slice approximations [8, 9, 12, 30], leading to inaccuracies in the 3D reconstruction.

Pioneering works in reflection-mode DT [13, 15] have shown promising results using the discrete dipole approximation (DDA), which models multiple scattering by discretizing the structure into a finite number of dipoles. While DDA provides a more accurate representation of

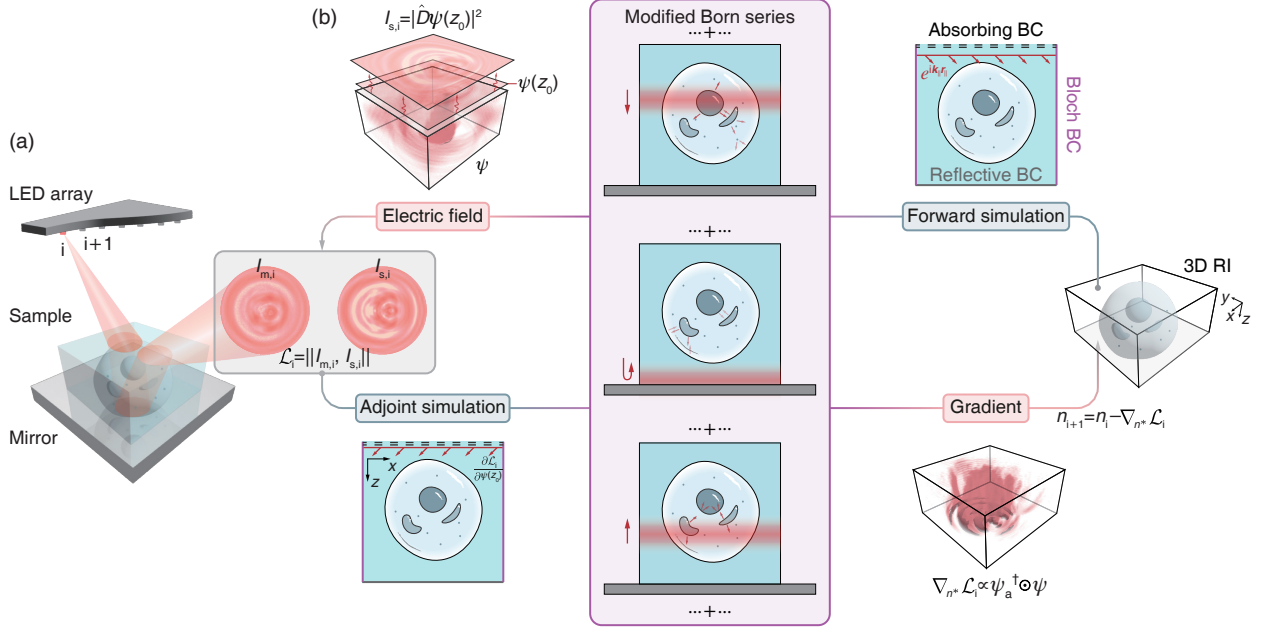


Fig. 1. Overview of the reflection-mode DT technique. (a) A reflection-mode LED array microscope captures brightfield intensity measurements from multiple illumination angles on a sample placed on a reflective substrate. (b) The reconstruction algorithm iteratively estimates the 3D RI distribution through forward and backward processes. The forward process uses the modified Born series to simulate multiple scattering with appropriate boundary conditions, while the adjoint method computes the gradient in the backward process.

complex scattering, its computational cost scales significantly with the number of dipoles, limiting its efficiency for large structures or high-contrast materials. Similarly, full-wave simulation methods such as finite-difference time-domain (FDTD) [24] can model the entire scattering process but are computationally expensive and impractical for real-time applications. On the other hand, single-scattering models in reflection-mode DT [20] are more computationally efficient but limited to imaging thin, weakly scattering samples.

To address these challenges, we develop a reflection-mode DT technique for imaging multiple-scattering samples on highly reflective substrates (Fig. 1(a)). This approach incorporates several key innovations: the modified Born series (MBS) as the forward model, Bloch boundary conditions (BC) and perfect electric conductor (PEC) BC to handle oblique incidence and substrate reflections, and the adjoint method (AM) [10, 17] for efficient gradient computation in solving the inverse-scattering problem (Fig. 1(b)).

We employ MBS [1], a robust and fast-converging multiple-scattering model for solving the inhomogeneous Helmholtz equation. MBS has demonstrated state-of-the-art performance in transmission-mode DT for complex biological samples [26]. It iteratively refines the scattering solution until convergence without relying on approximations. Unlike the conventional Born series [25], which suffers from convergence issues, MBS introduces a preconditioner and a localized Green's function that reduces the interaction radius to a spherically decayed region, ensuring fast and stable convergence. Additionally, MBS rigorously incorporates both forward and backward scattering components, making it well-suited for accurately modeling the complex wave interactions encountered in reflection-mode measurements.

In MBS, BC plays a crucial role in accurately simulating wave propagation, especially in complex scattering environments. An absorbing BC has been implemented in MBS using ultra-thin boundary layers [2], which efficiently minimizes reflections at the boundaries with low computational and memory overhead. However, to extend the applicability of MBS to reflection-mode conditions, particularly for imaging setups with highly reflective substrates like semiconductor wafers, we introduce two additional BCs: the Bloch BC and the PEC BC.

To implement the Bloch BC, we propose the use of acyclic convolution (ACC) [2, 11], which allows for a padding-free realization of Bloch BC within MBS. The Bloch BC is essential for handling oblique incidences by ensuring periodic BCs in systems with phase shifts. ACC achieves this by introducing an extra phase ramp and applying a shift to the Green’s function, thereby modulating the phase delay of the field that leaks from the boundaries. This mechanism allows the Bloch BC to accurately represent wave propagation at arbitrary angles.

To simulate the strong reflections from the substrate in reflection-mode DT, we introduce a self-adaptive PEC BC within MBS. While the original MBS can model reflections using high RI materials, this approach increases computational complexity due to the need for finer grids. To simplify this, the PEC BC simulates lossless reflection by approximating the substrate as generating an equivalent surface current, mimicking the behavior of a reflective surface. At each MBS iteration, a correction cancels the tangential component of the surface electric field, ensuring accurate boundary behavior while significantly reducing computational demands.

To reduce the memory costs associated with gradient calculation in our technique, we employ AM instead of traditional chain-rule-based methods. AM is a highly efficient technique for computing gradients in inverse problems constrained by partial differential equations (PDEs) and has been applied in areas like nanophotonic inverse design [22] and transmission-mode DT [23]. Unlike chain-rule methods, which require storing all the intermediate fields at each iteration, AM allows computing the gradient using only the final scattering field, leading to significant memory savings. AM achieves this by solving an additional adjoint problem that is linked to the original forward problem. This makes AM particularly advantageous for complex, iterative models like MBS, where memory management is crucial for scaling up to large-scale problems.

Our technique builds on the emerging strategy of DT that utilizes only intensity measurements [8, 9, 12], eliminating the need for a dedicated interferometric setup. Instead of capturing interferograms to retrieve full-field information, our method addresses the inverse-scattering problem using “phaseless” intensity measurements from multiple illumination angles. We validate the technique through both simulations and experiments. In simulations, we reconstruct synthetic 3D RI distributions and analyze the information captured by forward and backward scattering components in the 3D Fourier space. Our results reveal that in finite numerical aperture (NA) measurements, backscattered signals introduce high-frequency axial artifacts, for which we propose a filtering technique to mitigate. For experimental validation, we employ our previously developed reflection-mode LED array microscope to capture brightfield measurements [33]. We demonstrate the technique’s effectiveness by imaging a dual-layer resolution target sample and reconstructing high-resolution phase structures obscured by a strongly scattering random fiber structure, simulating realistic metrology and inspection tasks.

These results underscore the method’s potential for high-resolution 3D reconstructions, even in challenging, strongly scattering environments, positioning it as a promising tool for emerging metrology and inspection applications.

2. Theory and method

2.1. Overview of our reflection-mode DT technique

Our reflection-mode DT technique aims to characterize the 3D RI distribution of a structure placed on a highly reflective substrate, such as a silver mirror, as illustrated in Fig. 1(a). To perform the reconstruction, we first measure the scattered field intensities under varying illumination angles

$I_{m,i}$, achieved using a programmable LED array. The illumination direction is calibrated using the method from [33, 34].

Once the intensities are collected, the 3D RI distribution is reconstructed by solving the inverse scattering problem, as shown in the iterative loop in Fig. 1(b). This process involves two main stages: the forward and backward processes.

In the forward process, MBS serves as the forward model, starting with an initial guess of the RI (typically the background RI). MBS iteratively refines the electric field ψ , incorporating multiple scattering and handling reflections from the substrate. After convergence, the field on the simulation domain's surface ($z = z_0$) is projected onto the camera plane through a detection operator \hat{D} . The simulated intensity $I_{s,i}$ is compared with the measured data, and the loss function \mathcal{L}_i is computed.

In the backward process, AM is used to compute the RI gradient for updating the distribution. An adjoint simulation is performed, generating an adjoint field ψ_a with a mirrored incident direction. The RI gradient is obtained by element-wise multiplication of ψ_a and ψ . After each gradient descent step, the updated RI is used for the next iteration with new measurements under different illumination conditions. This process continues until the loss function converges.

This outlines the main workflow of our reflection-mode DT reconstruction strategy. Further details are elaborated in the following sections.

2.2. Modified Born series (MBS)

MBS is an efficient and rigorous forward model for solving the inhomogeneous Helmholtz equations, which in its discrete form is expressed as,

$$\nabla^2 \psi + k^2 \psi = -S, \quad (1)$$

where $\psi \in \mathbb{C}^{N \times 3}$ donates the electric field, $S \in \mathbb{C}^{N \times 3}$ is the electric current source at wavelength λ and $k = \text{diag}(n)k_0$ is the wavenumber in an isotropic medium with $n \in \mathbb{C}^{N \times 1}$ representing the RI distribution, $\text{diag}(\cdot)$ the diagonal matrix, and $k_0 = 2\pi/\lambda$. By using Green's function, its solution can be formulated as,

$$\psi = \mathcal{G}V\psi + \mathcal{G}S, \quad (2)$$

where $\mathcal{G} \equiv \mathcal{F}^{-1}[\tilde{\mathbf{g}}_B(\mathbf{q}) \cdot \mathcal{F}(\cdot)]$ is the Green's function operator implemented using the angular spectrum method, and $V = k - n_b^2 k_0^2$ is the scattering potential. \mathcal{F} and \mathcal{F}^{-1} donate the Fourier and inverse Fourier transforms, $\tilde{\mathbf{g}}_B \in \mathbb{C}^{N \times N \times 3 \times 3}$ is the Fourier transform of the dyadic Green's function in the background medium with RI n_b and \mathbf{q} denotes the spatial frequency coordinates.

Expanding ψ based on Eq. (2) recursively leads to the conventional Born series,

$$\psi_B(\mathbf{r}) = [\mathbf{I} + \mathcal{G}V + \mathcal{G}V\mathcal{G}V + \dots] \mathcal{G}S, \quad (3)$$

where $\mathbf{r} \equiv (\mathbf{r}_{\parallel}, z)$ denotes the spatial coordinates, and \mathbf{I} is the identity matrix. However, the conventional Born series suffers from divergence issues during recursions. To address this, G. Osnabrugge et al. introduced a preconditioner $\gamma = iV/\eta$ and modified the Green's function as $\tilde{\mathbf{g}}_M(\mathbf{q}) = (\mathbf{I} - \mathbf{q}\mathbf{q}^T)/(|\mathbf{q}|^2 - n_b^2 k_0^2 - i\eta)$, reducing its influence radius from the original entire simulation domain to a spherically decaying region, whose effect is illustrated by the red band matching as the series order increases in Fig. 1(b) (see mathematical details in Section 1 in Supplement 1). The scattering potential is modified as $V_M = V - i\eta$ to compensate for the effective energy loss. The resulting MBS is expressed as:

$$\psi_M = [\mathbf{I} + \mathbf{M} + \mathbf{M}^2 + \dots] \gamma \mathcal{G}_M S, \quad (4)$$

where $\mathbf{M} \equiv \gamma \mathcal{G}_M V_M - \gamma + \mathbf{I}$ and $\mathcal{G}_M \equiv \mathcal{F}^{-1}[\tilde{\mathbf{g}}_M(\mathbf{q}) \cdot \mathcal{F}(\cdot)]$.

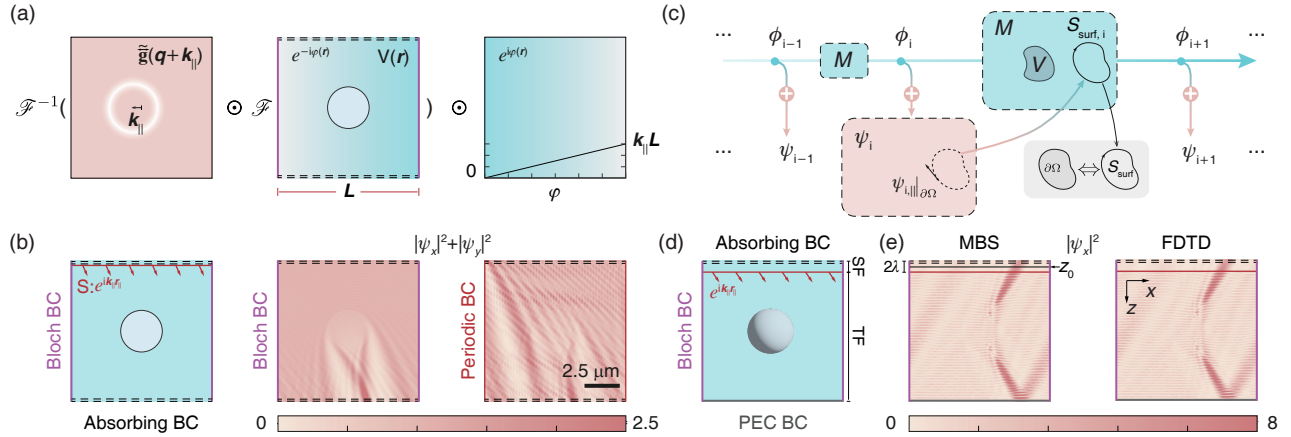


Fig. 2. (a) Padding-free Bloch BC implementation in MBS: 1) apply a phase ramp $e^{-ik_{\parallel} \cdot r_{\parallel}}$ to the entire simulation domain, 2) compute the scattered field using a frequency-shifted Green's function $\tilde{g}_M(\mathbf{q} + \mathbf{k}_{\parallel})$, 3) re-modulate with a reverse phase ramp $e^{ik_{\parallel} \cdot r_{\parallel}}$ in real space. (b) Comparison of 2D simulations between Bloch and periodic BCs under oblique incidence. Simulation parameters: $L = 10 \mu\text{m}$, $\lambda = 532 \text{ nm}$, $n_b = 1.336$; the scatterer has a radius of $1.5 \mu\text{m}$ with a RI of 1.461. (c) Computational graph for implementing PEC BC in MBS, realized by a surface current source S_{surf} . (d) MBS simulation domain setup. TF: total field, SF: scattered field. The z_0 plane is positioned midway between the top absorbing boundary and the one-way source for extracting the scattered field. (e) Comparison of 3D simulations between MBS and FDTD with matching BCs.

2.3. Bloch boundary condition for MBS

To replicate real experimental conditions within a finite simulation domain, BCs are commonly applied to prevent artificial reflections and unwanted scattering. A widely used method is the absorbing BC, which absorbs the light waves as they exit the simulation domain in an open system. In MBS, absorbing BCs have been implemented using ultra-thin boundary layers [2], offering low computational and memory costs. To extend MBS for reflection-mode conditions, we further introduce two additional BCs, including Bloch BC (Fig. 2(a)) and PEC BC (Fig. 2(c)).

Bloch BC [36] is commonly used in numerical methods like FDTD to handle the oblique incidence wave $e^{ik_{\text{in}} \cdot \mathbf{r}}$, where $\mathbf{k}_{\text{in}} = [\mathbf{k}_{\parallel}, k_z]$. In FDTD, implementing Bloch BC is straightforward: a constant Bloch phase factor, $e^{\pm ik_{\parallel} \cdot L}$, is first applied to the boundary field before copying it to the opposite side. Here, L represents the dimensions of the simulation domain, and the + and - signs correspond to the right and left boundaries, respectively. This ensures the correct phase shift for waves exiting and re-entering the simulation domain.

The most straightforward way of applying the Bloch BC based on the angular spectrum method, with a similar way as in FDTD, requires first padding regions at least the same size as the simulation domain before applying the Bloch phase factor to the padded region, in order to both ensure the correct phase shift for waves exiting and re-entering the simulation domain (see details in Section 2 in Supplement 1). However, this approach results in too much memory overhead.

To overcome this, we propose adapting the ACC method [2, 11] to achieve a *padding-free* Bloch BC in MBS, as illustrated in Fig. 2(a). First, a phase ramp $e^{-ik_{\parallel} \cdot r_{\parallel}}$ is applied to the entire simulation domain in the real space to effectively demodulate the field before performing discrete Fourier transform (DFT). Correspondingly, we use a frequency-shifted Green's function

$\tilde{\mathbf{g}}_{\text{M}}(\mathbf{q} + \mathbf{k}_{\parallel})$ to compute the scattered field. Finally, the scattered field is re-modulated by $e^{i\mathbf{k}_{\parallel} \cdot \mathbf{r}_{\parallel}}$ in the real space. Accordingly, the modified Green's function operator is

$$\mathcal{E}_{\text{Bl}} \equiv \mathcal{F}_{\text{Bl}}^{-1} \left[\tilde{\mathbf{g}}_{\text{M}}(\mathbf{q} + \mathbf{k}_{\parallel}) \cdot \mathcal{F}_{\text{Bl}}(\cdot) \right], \quad (5)$$

where $\mathcal{F}_{\text{Bl}}(\phi) \equiv \mathcal{F}(\phi e^{-i\mathbf{k}_{\parallel} \cdot \mathbf{r}_{\parallel}})$ and $\mathcal{F}_{\text{Bl}}^{-1}(\tilde{\phi}) \equiv \mathcal{F}^{-1}(\tilde{\phi}) e^{i\mathbf{k}_{\parallel} \cdot \mathbf{r}_{\parallel}}$. This method ensures that the fields leaking from the boundaries automatically satisfy the Bloch BC, without the need for additional padding or calculations. In Fig. 2(b), 2D MBS simulations on a circular scatterer with Bloch and periodic BCs are compared. The periodic BC introduces strong artifacts due to the mismatch between the incident field at the two ends. In contrast, our proposed padding-free Bloch BC ensures that the re-entering field seamlessly matches the internal field. Note that ACC is not limited to implementing Bloch BC in MBS; it can also be easily extended to other forward models based on the angular spectrum method, such as angular spectrum diffraction, single-scattering, and multi-slice methods.

2.4. Perfect Electric Conductor (PEC) Boundary Condition for MBS

We implemented a self-adaptive PEC boundary in MBS to simulate strong reflections from a substrate. While MBS can accurately model reflection at an interface, incorporating a high RI substrate typically requires finer grids and smaller propagation steps, significantly increasing computational complexity. To simplify this, we use a PEC boundary as a lossless reflection model for the substrate interface, providing insights into reflection-mode DT without excessive computational demands.

Based on the equivalence principle [35], a PEC boundary is equivalent to a surface electric current source \mathbf{S}_{surf} on the boundary surface $\partial\Omega$. Therefore, applying a PEC BC is converted to solving for \mathbf{S}_{surf} such that $\hat{\mathbf{n}} \times \boldsymbol{\psi}(\mathbf{r})|_{\partial\Omega} = 0$.

At each MBS iteration, we incrementally add a surface current source $\mathbf{S}'_{\text{surf},i} \propto \hat{\mathbf{n}} \times \boldsymbol{\psi}(\mathbf{r})|_{\partial\Omega}$, as shown in Fig. 2(c). The recursive formula for the i -th MBS scattering field $\boldsymbol{\phi}_i$ can be written as

$$\boldsymbol{\phi}_{i+1} = \mathbf{M}\boldsymbol{\phi}_i + i\gamma\mathcal{E}_{\text{M}} \left[\boldsymbol{\psi}_i|_{\partial\Omega} - \hat{\mathbf{n}} \cdot \boldsymbol{\psi}_i|_{\partial\Omega} \right], \quad (6)$$

where $\hat{\mathbf{n}}$ is the normal vector of $\partial\Omega$ and $\boldsymbol{\psi}_i$ is the total field at the i -th iteration. By defining the added surface current source as $\mathbf{S}_{\text{surf},i}(\mathbf{r}) = i \left[\boldsymbol{\psi}_i|_{\partial\Omega}(\mathbf{r}) - \hat{\mathbf{n}} \cdot \boldsymbol{\psi}_i|_{\partial\Omega} \right]$, the induced electric field cancels the tangential components of the total field estimated on the PEC surface. Moreover, when the PEC BC is fully satisfied, the added source will vanish automatically, making this a self-adaptive mechanism for integrating the PEC BC in MBS. (see mathematical details in Section 2 in Supplement 1).

2.5. MBS simulation setup

A typical simulation domain in our framework is shown in Fig. 2(d). The four side walls are configured with Bloch BCs (purple lines), the bottom plane is assigned a PEC BC (gray line), and the top plane is set with an absorbing BC (double dashed line).

In reflection mode, unlike transmission mode, incident and scattered wave components intermingle within the simulation domain, creating an axial standing wave, as illustrated in Fig. 2(d). This overlap complicates field analysis, making it essential to isolate the scattered field from the total field for accurate interpretation. To achieve this, the simulation is divided into distinct regions for the total and scattered fields.

A one-way source is introduced to isolate the scattered field by generating a plane wave propagating in a single direction. This is achieved using a dual-layer source (red line), consisting of two staggered planar sources placed one grid point apart in the z -direction with an interval Δz . In the lateral direction, each planar source has a phase distribution $e^{i\mathbf{k}_{\parallel} \cdot \mathbf{r}_{\parallel}}$ to produce the desired

oblique incidence. The bottom source also includes an additional phase factor $-\exp(-ik_z\Delta z)$, canceling any backward-propagating incident waves. The planar source is positioned two wavelengths below the absorbing boundary, with its k_z aligned along the positive z -axis.

The region between the source and the PEC boundary serves as the total-field region, where structures are placed to simulate scattering. The area between the source and the absorbing boundary is the scattered-field region, containing only the pure scattered field from the structure and substrate. The z_0 plane is positioned in the middle of this gap to capture the scattered field, which is then projected onto the camera plane. The two-wavelength gap effectively eliminates potential evanescent waves near the source or boundary, allowing for accurate analysis of the scattered field.

To validate our method, we simulate the scattering field of a 3D sphere positioned near a PEC boundary, and benchmark the result against FDTD. The spherical scatterer, with a radius of $1.5 \mu\text{m}$ and a RI of 1.461, is placed $6 \mu\text{m}$ above the PEC boundary within a background medium of RI 1.336. The simulation domain, measuring $12 \mu\text{m}$, is discretized into 20 nm voxels for both MBS and FDTD simulations. The scatterer is illuminated by circularly polarized light with a wavelength of 532 nm at an incident angle of 30° . Fig. 2(e) compares the x - z profiles of the simulated electric fields obtained from MBS and FDTD (additional comparisons are provided in Supplement 1). The simulations show strong agreement, capturing the full scattering lobes, reflections from the substrate, and standing wave patterns in both cases.

2.6. Detection Operator

After the forward process of MBS, the calculated scattered field at the top slice, $\psi_M(z_0)$, is projected onto the camera plane using a detection operator \hat{D} , as illustrated in Fig. 3(a). The detection operator \hat{D} models the imaging process in the microscopy system to simulate the captured intensity $I_{s,i}$. First, $\psi_M(z_0)$ is numerically propagated to the focal plane of the objective lens and modulated by its pupil function, which ideally acts as a hard aperture with a radius defined by the NA. Finally, the intensities of each polarized component are summed to produce the simulated intensity $I_{s,i}$. (see details in Section 3 in Supplement 1).

2.7. Adjoint method

To solve the inverse scattering problem, we define a loss function \mathcal{L}_i that quantifies the difference between the simulated intensity $I_{s,i}$ and the measured intensity I_m for each LED illumination:

$$\mathcal{L}_i = \|I_{s,i} - I_{m,i}\|_2^2, \quad (7)$$

where $\|\cdot\|_2$ denotes the ℓ_2 -norm. Since MBS is a nonlinear forward model, we minimize \mathcal{L}_i using a gradient descent approach.

In Wirtinger calculus [38], the gradient $\nabla_{n^*}\mathcal{L}_i$ is computed to update the RI distribution in order to minimize the real-valued loss function \mathcal{L}_i . To reduce memory costs associated with storing intermediate fields, we employ AM rather than traditional chain-rule-based methods. The gradient with AM can be expressed as

$$\nabla_{n^*}\mathcal{L}_i = [2k_0^2 \text{diag}(\mathbf{n}) \cdot \psi_a^* \circ \psi_M]^\dagger, \quad (8)$$

where ψ_a is the solution to the adjoint simulation, given by

$$\nabla^2\psi + k_0^2 \text{diag}(\epsilon^*)\psi = -\left(\frac{\partial\mathcal{L}_i}{\partial\psi_M}\right)^\dagger, \quad (9)$$

This adjoint simulation of MBS (see details in Section 4 in Supplement 1) only requires the field at the z_0 -plane to define \mathcal{L}_i , making $(\partial\mathcal{L}_i/\partial\psi_M)^\dagger \in \mathbb{C}^{N \times 3}$ a plane-shaped source located at the

z_0 -plane. If Bloch BCs are used in the forward simulation, the Bloch wave vector \mathbf{k}_{Bl} must be reversed in the adjoint simulation.

Since AM is derived from the Helmholtz equation (Eq. (1)), Eq. (8) serves as a universal formula for calculating gradients across all forward models. Moreover, Eq. (8) defines the minimal information required to calculate the gradient in a scattering problem. While gradients in MBS can be computed using chain-rule-based backpropagation, this approach requires storing all intermediate fields generated during each MBS iteration, resulting in significant memory overhead, especially given MBS's volumetric iterative nature. In contrast, using AM for gradient calculation reduces memory demands, as only the final scattering field ψ_{M} needs to be retained. This leads to substantial memory savings.

For validation, we computed the gradient in a 2D simulation using both AM and the chain rule, with the latter implemented via PyTorch's automatic differentiation module. Both simulations were run on an Nvidia RTX 4090 24 GB graphics card to compare memory and time consumption. The gradient results, shown in Fig. 3(b), indicate that the gradients calculated using AM closely align with those from the chain rule. However, the difference in computational cost is significant: AM requires only 504 MB of memory and completes in 157 ms, while the chain-rule-based method, which must store all intermediate fields, consumes 20.29 GB and takes 527 ms.

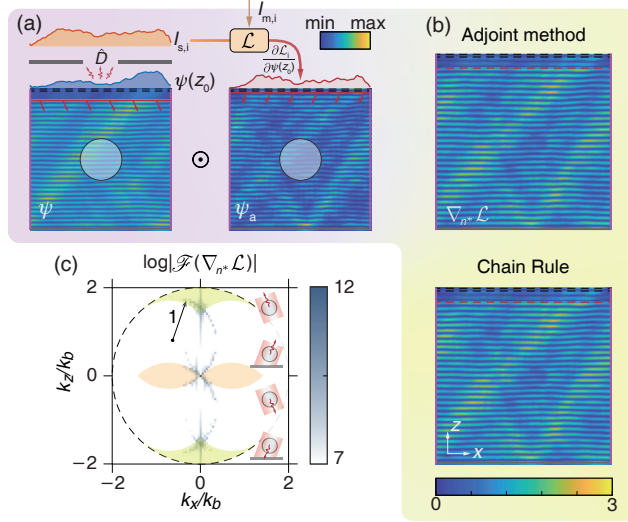


Fig. 3. (a) Illustration of AM used for calculating the gradient in a 2D simulation of scattering from a circular scatterer placed on a mirror. Simulation parameters: wavelength $\lambda = 632$ nm, background RI $n_b = 1.336$, domain size $L = 10$ μm , incident angle $\theta = 40^\circ$, and NA = 0.95 in air. The scatterer radius is 1.5 μm with an RI of 1.361. (b) Comparison of gradients calculated using AM and the chain rule method. (c) Fourier spectrum of the calculated gradient, with orange and yellow masks indicating forward and backscattering regions based on the single-scattering model, respectively.

3. Results

3.1. Information Analysis in Forward and Backward Scattering

Before performing reconstruction tasks, we first analyze the information captured by reflection-mode DT by interpreting the gradient derived from the loss function. In real space, the gradient reveals lateral stripes with strong oscillations along the axial direction. These axial oscillations correspond to two bright regions in the high axial-frequency domain around $k_z = \pm 2k_b$ in the

Fourier spectrum, as shown in Fig. 3(c).

To guide our interpretation, we plot the Fourier support based on the single-scattering model [37], with orange and yellow masks representing forward and backscattering contributions, respectively. Although our model includes multiple scattering, which includes higher-order effects, the alignment of the high axial frequency components with the backscattering region predicted by the single-scattering model indicates that the observed axial oscillations originate from captured backscattered signals. Notably, our multiple scattering model also predicts frequency components extending beyond the single-scattering region, as seen in Fig. 3(c). In contrast, forward scattering corresponds to the slowly varying components in the gradient, aligning with the low-frequency region predicted by the single-scattering model, while multiple scattering introduces additional frequency components extending beyond this region.

3.2. Numerical Validation and Spectral Filtering

We first validate the reflection-mode DT technique in simulation by implementing the gradient descent algorithm to reconstruct the 3D RI distribution from simulated intensity measurements. In our simulations, we used a light wavelength of 632 nm and a pupil with a finite NA of 0.95. Circular polarization was employed in both simulation and experiments to mimic the isotropic and unpolarized illumination from the LED.

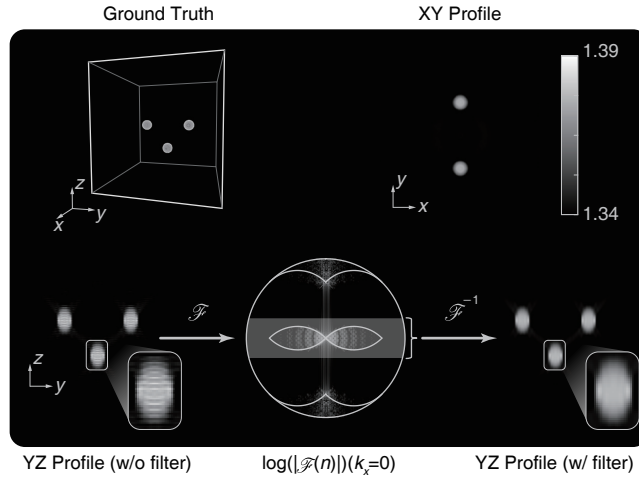


Fig. 4. Reflection-mode DT reconstruction results for simulated bead-shaped scatterers (RI $n = 1.39$, radius $1 \mu\text{m}$). Simulation parameters: $\lambda = 632 \text{ nm}$, $n_b = 1.34$, NA = 0.95. A total of 138 illumination angles are used, arranged in 7 concentric circles with equal spacing in NA, with the outermost circle corresponding to 0.95 NA. A low-pass filter was applied to remove high-frequency artifacts caused by backscattering, resulting in clearer reconstructions.

The reflection-mode DT reconstruction was first tested on bead scatterers, with the reconstructed RI results shown in Fig. 4. Due to the high axial frequency features present in the gradients (Fig. 3(b)), the reconstructed 3D RI also displayed dense stripe artifacts along the z -axis. These artifacts arise from high-frequency backscattering components, which, while present in the gradient, cannot be fully utilized to enhance axial resolution due to the limited information content in intensity-only measurements in reflection-mode DT without interferometric gating [39].

To address this, we apply a low-pass filter along the axial dimension, cropping the Fourier spectrum of the reconstructed RI. This filter retains only the low-frequency region around the forward scattering support, where the most reliable information is concentrated, as illustrated in the

middle-bottom panel of Fig. 4. By selectively filtering out the high-frequency axial components, the dense stripe artifacts are effectively removed, resulting in a clearer RI reconstruction, as shown in the right-bottom panel of Fig. 4.

3.3. Experiments

Our experimental setup is based on our previously developed reflection-mode LED microscope [33], as shown in Fig. 5(a). A $10\times/0.28$ NA (Mitutoyo Plan Apo Infinity Corrected Long WD) objective lens collects the scattered signals. For oblique illumination, a 25-LED array (Kingbright) is positioned at the focal plane of a $4-f$ system and relayed to the back focal plane of the objective. The LED array consists of a central LED and two concentric rings, with the outermost ring matching the objective NA, providing illumination NAs of 0.14 and 0.28 for the rings. Each LED illuminates the sample as a plane wave with a central wavelength of 632 nm and a 20 nm bandwidth. The intensity is captured by a camera (Imaging Source, DMK38UX541, $2.74\ \mu\text{m}$ pixel size).

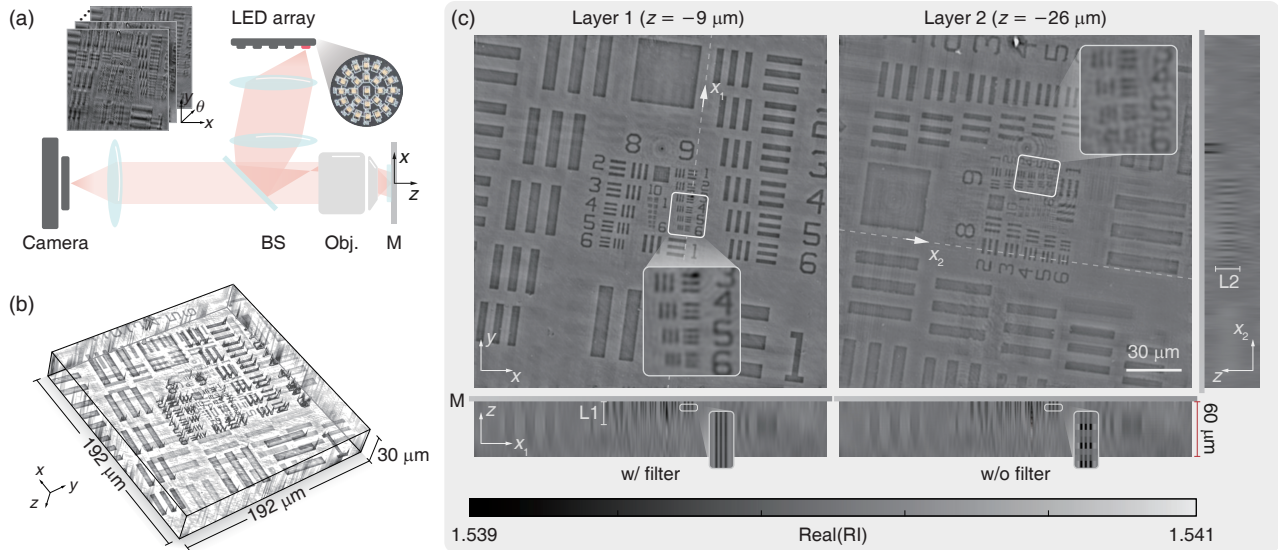


Fig. 5. Reflection-mode DT of a two-layer resolution target sample. (a) Schematic of our reflection-mode DT setup. BS: beam splitter, Obj: objective lens, M: mirror. Illumination is provided by a 25-LED array with a central wavelength of 632 nm. The illumination NAs of the two LED rings are 0.14 and 0.28. Inset: captured 2D intensity images from different illumination angles. (b) 3D rendering of the reconstruction result of the dual-layer resolution target ($z \in [0, 30\ \mu\text{m}]$). (c) x - y , x_1 - z , and z - x_2 cross-sections of the reconstructed RI distribution. The gray dashed lines, x_1 and x_2 , intersect Group 9 in Layer 1 and Group 8 in Layer 2, illustrating the z cross-sections. High-frequency artifacts from backscattering are visible in the experimental reconstruction, and a low-pass filter was applied to remove them, with a comparison shown in the zoomed-in inset of the x_1 - z cross-sections. The zoomed-in inset of the x - y cross-sections highlights the reconstructed regions around Element 5 in Group 9 for both layers, demonstrating diffraction-limited lateral resolution in both layers. The x - z and z - y cross-sections show the achieved axial resolution in resolving the two-layer structure.

3.3.1. Two-layer phase resolution target

We first image a dual-layer structure to demonstrate the capability of reflection-mode DT in resolving complex 3D structures, addressing challenges in conventional microscopy where scattering from out-of-focus regions obscures structures at different depths. This issue is particularly severe in reflection-mode, as light undergoes both forward and backward scattering events, compounding the scattering effects. Our reflection-mode DT technique addresses these limitations by reconstructing the 3D structure through solving an inverse scattering problem.

For validation, we fabricated a dual-layer phase resolution target sample. Two different targets were replicated in resin, with a nominal axial separation of $17.5\ \mu\text{m}$ between the layers. The nominal height of Layer 1 is 200 nm, while Layer 2 is 100 nm. The original master target used for replication is the Quantitative Phase Target (Benchmark Technologies). The two layers were stacked on a silver mirror and aligned at the center. The top layer was rotated by 90 degrees, and the space between the layers was filled with glycerin before being sealed with a cover glass.

The raw measurements, as illustrated in the inset of Fig. 5(a), include contributions from double passing through the sample due to the substrate. This results in significant overlap of phantom images from each layer in the measurement.

The reconstructed volume extends from the mirror surface to $60\ \mu\text{m}$ above, with a field of view (FOV) of $192\ \mu\text{m} \times 192\ \mu\text{m}$. The volume is discretized on a uniform grid with 136 nm spacing in all three dimensions. The 3D rendered RI reconstruction ($z \in [0, 30\ \mu\text{m}]$) is shown in Fig. 5(b), while cross-sections of the reconstructed RI are provided in Fig. 5(c).

The zoomed-in x - y profile inset demonstrates that our reflection-mode DT technique significantly enhances lateral resolution in both layers. In both Layer 1 and Layer 2, features in Group 9, Element 5 (1230 nm period) are clearly resolved, as shown in the zoomed-in inset of Fig. 5(c). This confirms that the reconstruction achieves the expected synthetic NA of 0.56, corresponding to a theoretical diffraction-limited resolution of 1128 nm, representing a $2\times$ improvement in NA over single-LED brightfield measurements.

The z cross-section along the x_1 and x_2 (marked as gray dashed lines) are illustrated in the surrounding panels. In the x_1 - z profile, horizontal stripe artifacts from backscattering are visible. Applying an axial low-pass filter effectively removes these artifacts, resulting in a clearer x_1 - z profile of the RI reconstruction, as shown in the zoomed-in inset. The x_1 - z and z - x_2 cross-sections demonstrate the achieved axial resolution in resolving the two-layer structure. The current axial resolution and quantification of RI is limited by the limited NA of our system, similar to the observations in transmission DT observations [8]. The limited axial resolution causes the reconstructed RI distributions of both layers to extend along the z -axis, spanning approximately $24\ \mu\text{m}$, which aligns with the expected axial resolution based on the Fourier coverage from the low-frequency band ($24.6\ \mu\text{m}$). Since the nominal height of Layer 2 is half of that of Layer 1, the RI distribution in Layer 2 exhibits a lower contrast in the x - y profile. Averaging the RI difference between target and background, $\langle \Delta n \rangle = \overline{n - n_b}$, in Group 8 elements, the contrast ratio between Layer 1 and Layer 2, $\langle \Delta n_1 \rangle / \langle \Delta n_2 \rangle$, is 1.82, close to the nominal height ratio of 2. Future improvements in axial resolution and quantification of RI can be achieved with a higher-NA objective.

3.3.2. Phase spoke target behind random fibers

Finally, we apply reflection-mode DT reconstruction to image structures obscured by strongly scattering occluders. Such occluders, such as scratches, dust, or overlapping elements, act as irregular strong scatterers, causing significant distortions and challenging direct inspection. Reflection-mode DT provides a novel approach for visualizing structures behind these occluders.

To mimic an obscured sample, we use a torn piece of lens tissue as an occluder. The tissue, made of coarse fibers, strongly scatters light, creating a semi-transparent but highly distorted view, making it ideal for this purpose. For sample preparation, a resin-copied spoke resolution

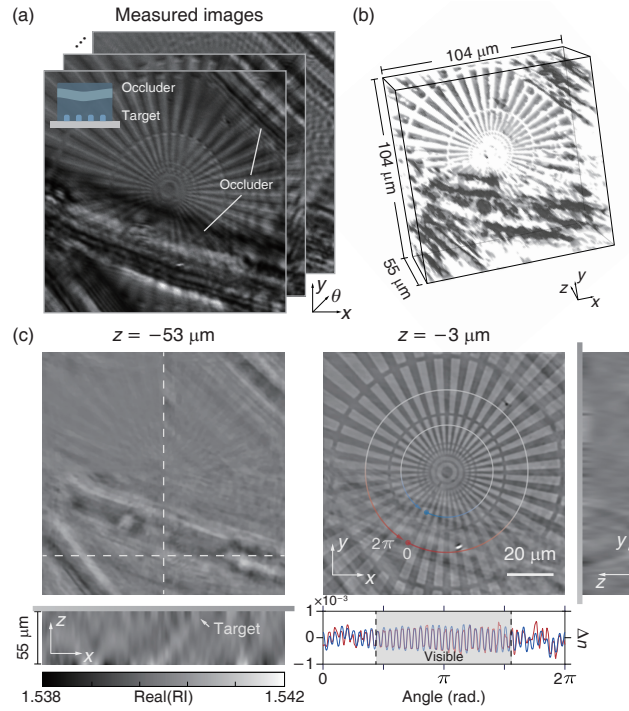


Fig. 6. Reflection-mode DT of a phase spoke target behind random fibers. (a) Example measurements under different illumination angles. (b) 3D rendering of the reconstruction. (c) Cross sections of reconstructed 3D RI. After reconstruction, most of the previously occluded spoke patterns are clearly resolved. Bottom: Difference between reconstructed RI and background RI (1.54) along two circular traces marked in the x - y profile. The area between the dashed lines represents the visible region in measurements, while the areas on either side correspond to the occluded regions.

target is affixed to a mirror surface with a piece of lens tissue secured above it with resin. Nominal height of the target structure is 300 nm. Approximately, the separation between the fiber plane and the target is 45 μm .

The same experimental setup is used to capture intensities at different illumination angles, with example images shown in Fig. 6(a). In the captured data, parts of the target are obscured by random fibers, causing significant scattering and distortion, making those resolution features nearly unobservable.

Applying reflection-mode DT reconstruction allows for separation of the target and occluders along the z -direction in the reconstructed 3D RI, as illustrated in Fig. 6(b). The reconstructed volume extends from the mirror surface to 55 μm above, with an FOV of 104 $\mu\text{m} \times 104 \mu\text{m}$. Cross-sections of the 3D reconstructed RI are shown in Fig. 6(c). In the x - y profile near the mirror surface, the occluded spoke resolution features are now clearly visible, with edges aligned seamlessly with uncovered regions. Difference between reconstructed RI and background RI (1.54), Δn , along two circular traces is further plotted at the bottom for detailed comparison, with previously obscured regions highlighted in blue and red in the x - y cross-sectional image. While not as sharp as uncovered areas, the previously distorted structures are now distinctly visible.

In this reconstruction, 3D total variation (TV) regularization [40] is applied to enhance the result by suppressing the reconstruction artifacts. TV regularization is applied to the RI distribution after each epoch of the gradient descent algorithm. To prevent high-frequency

artifacts from backscattering from interfering with the regularization, a low-pass filter is first applied to the RI distribution to remove these artifacts before performing TV regularization (see details in Section 5 of Supplement 1).

This result underscores the potential of our technique for achieving accurate inspection of structures on substrates obscured by defects or overlapping elements, presenting a promising solution for challenging inspection scenarios.

4. Conclusion and Discussion

In conclusion, we presented a novel DT technique that enables 3D RI reconstruction from intensity-only measurements on reflective substrates. This approach combines MBS as the forward model with AM for efficient gradient calculation, tailored to capture complex multiple scattering in challenging metrology and inspection scenarios. To accurately model reflection measurements, we introduced Bloch and PEC BCs within MBS, facilitating accurate reconstruction on reflective surfaces. By using AM, we address memory demands in gradient computation, storing only the total scattering field and providing a practical approach for complex scattering models.

Validated through both simulation and experiment, our method successfully reconstructed depth-resolved features in dual-layer resolution targets and structures obscured by scattering fibers, achieving diffraction-limited 3D resolution.

This DT technique opens new opportunities for DT in semiconductor metrology, photonic devices, and microelectromechanical systems. Its ability to reconstruct 3D RI distributions on reflective substrates offers a promising solution for wafer inspection, deep defect detection, and optical coatings monitoring. Incorporating Bloch BC within MBS also paves the way for future applications in the inverse design of periodic nanophotonic structures.

Future work will focus on extending the DT framework to handle more challenging highly scattering structures, such as silicon-based architectures, for advanced metrology tasks. Additionally, since our forward model is vectorial, this strategy is also suitable for polarization-resolved measurements, enabling characterization of anisotropic samples. Finally, optimizing the framework to reduce computational costs while maintaining high accuracy can further enhance its utility across a range of optical metrology challenges.

Funding. Samsung Global Research Outreach (GRO) program, and National Science Foundation (1846784).

Acknowledgment. The authors thank Boston University Shared Computing Cluster for providing the computational resources.

Disclosures. The authors declare no conflicts of interest.

Supplemental document. See Supplement 1 for supporting content.

References

1. Osnabrugge, Gerwin, Saroch Leedumrongwatthanakun, and Ivo M. Vellekoop. "A convergent Born series for solving the inhomogeneous Helmholtz equation in arbitrarily large media." *Journal of Computational Physics*, vol. 322, pp. 113–124, 2016.
2. Osnabrugge, G., Benedictus, M., & Vellekoop, I. M. (2021). Ultra-thin boundary layer for high-accuracy simulations of light propagation. *Optics Express*, 29(2), 1649-1658. <https://doi.org/10.1364/OE.407345>
3. Kim, T., Zhou, R., Mir, M., Babacan, S. D., Carney, P. S., Goddard, L. L., & Popescu, G. (2014). White-light diffraction tomography of unlabelled live cells. *Nature Photonics*, 8(3), 256-263.
4. Merola, F., Memmolo, P., Miccio, L., Savoia, R., Mugnano, M., Fontana, A., D'ippolito, G., Sardo, A., Iolascon, A., Gambale, A., & others. (2017). Tomographic flow cytometry by digital holography. *Light: Science & Applications*, 6(4), e16241.
5. Park, Y., Depeursinge, C., & Popescu, G. (2018). Quantitative phase imaging in biomedicine. *Nature Photonics*, 12(10), 578-589.
6. Ling, R., Tahir, W., Lin, H.-Y., Lee, H., & Tian, L. (2018). High-throughput intensity diffraction tomography with a computational microscope. *Biomedical Optics Express*, 9(5), 2130-2141.

7. Li, J., Matlock, A., Li, Y., Chen, Q., Zuo, C., & Tian, L. (2019). High-speed in vitro intensity diffraction tomography. *Advanced Photonics*, 1(6), 066004.
8. Chen, M., Ren, D., Liu, H.-Y., Chowdhury, S., & Waller, L. (2020). Multi-layer Born multiple-scattering model for 3D phase microscopy. *Optica*, 7(5), 394-403.
9. Zhu, J., Wang, H., & Tian, L. (2022). High-fidelity intensity diffraction tomography with a non-paraxial multiple-scattering model. *Optics Express*, 30(18), 32808-32821.
10. Piggott, A. Y., Lu, J., Lagoudakis, K. G., Petykiewicz, J., Babinec, T. M., & Vučković, J. (2015). Inverse design and demonstration of a compact and broadband on-chip wavelength demultiplexer. *Nature Photonics*, 9(6), 374-377.
11. Radhakrishnan, C., & Jenkins, W. K. (2010). Modified discrete Fourier transforms for fast convolution and adaptive filtering. In *Proceedings of 2010 IEEE International Symposium on Circuits and Systems* (pp. 1611-1614). IEEE.
12. Tian, L., & Waller, L. (2015). 3D intensity and phase imaging from light field measurements in an LED array microscope. *Optica*, 2(2), 104-111.
13. Mudry, E., Chaumet, P. C., Belkebir, K., Maire, G., & Sentenac, A. (2010). Mirror-assisted tomographic diffractive microscopy with isotropic resolution. *Optics Letters*, 35(11), 1857-1859.
14. Kang, I., Jiang, Y., Holler, M., Guizar-Sicairos, M., Levi, A. F. J., Klug, J., Vogt, S., & Barbastathis, G. (2023). Accelerated deep self-supervised ptycho-laminography for three-dimensional nanoscale imaging of integrated circuits. *Optica*, 10(8), 1000-1008.
15. Zhang, T., Ruan, Y., Maire, G., Sentenac, D., Talneau, A., Belkebir, K., Chaumet, P. C., & Sentenac, A. (2013). Full-polarized tomographic diffraction microscopy achieves a resolution about one-fourth of the wavelength. *Physical Review Letters*, 111(24), 243904.
16. Kim, K., Yoon, J., & Park, Y. K. (2016). Large-scale optical diffraction tomography for inspection of optical plastic lenses. *Optics Letters*, 41(5), 934-937.
17. Lalau-Keraly, C. M., Bhargava, S., Miller, O. D., & Yablonovitch, E. (2013). Adjoint shape optimization applied to electromagnetic design. *Optics Express*, 21(18), 21693-21701.
18. Ziemczonok, M., Kuś, A., & Kujawińska, M. (2022). Optical diffraction tomography meets metrology—Measurement accuracy on cellular and subcellular level. *Measurement*, 195, 111106.
19. Aidukas, T., Phillips, N. W., Diaz, A., Poghosyan, E., Müller, E., Levi, A. F. J., Aeppli, G., Guizar-Sicairos, M., & Holler, M. (2024). High-performance 4-nm-resolution X-ray tomography using burst ptychography. *Nature*, 632(8023), 81-88.
20. Matlock, A., Sentenac, A., Chaumet, P. C., Yi, J., & Tian, L. (2020). Inverse scattering for reflection intensity phase microscopy. *Biomedical Optics Express*, 11(2), 911-926.
21. Wolf, E. (1969). Three-dimensional structure determination of semi-transparent objects from holographic data. *Optics Communications*, 1(4), 153-156.
22. Molesky, S., Lin, Z., Piggott, A. Y., Jin, W., Vučković, J., & Rodriguez, A. W. (2018). Inverse design in nanophotonics. *Nature Photonics*, 12(11), 659-670.
23. Unger, K. D., Chaumet, P. C., Maire, G., Sentenac, A., & Belkebir, K. (2019). Versatile inversion tool for phaseless optical diffraction tomography. *JOSA A*, 36(11), C1-C8.
24. Taflove, A., Hagness, S. C., & Picket-May, M. (2005). Computational electromagnetics: The finite-difference time-domain method. In *The Electrical Engineering Handbook*, 3, 629-670. Elsevier Amsterdam, The Netherlands.
25. van Rossum, M. C. W., & Nieuwenhuizen, T. M. (1999). Multiple scattering of classical waves: microscopy, mesoscopy, and diffusion. *Reviews of Modern Physics*, 71(1), 313.
26. Lee, M., Hugonnet, H., & Park, Y. K. (2022). Inverse problem solver for multiple light scattering using modified Born series. *Optica*, 9(2), 177-182.
27. Zheng, G., Kolner, C., & Yang, C. (2011). Microscopy refocusing and dark-field imaging by using a simple LED array. *Optics Letters*, 36(20), 3987-3989.
28. Zheng, G., Horstmeyer, R., & Yang, C. (2013). Wide-field, high-resolution Fourier ptychographic microscopy. *Nature Photonics*, 7(9), 739-745.
29. Tian, L., Li, X., Ramchandran, K., & Waller, L. (2014). Multiplexed coded illumination for Fourier Ptychography with an LED array microscope. *Biomedical Optics Express*, 5(7), 2376-2389.
30. Kamilov, U. S., Papadopoulos, I. N., Shoreh, M. H., Goy, A., Vonesch, C., Unser, M., & Psaltis, D. (2015). Learning approach to optical tomography. *Optica*, 2(6), 517-522.
31. Waterman, P. C., & Truell, R. (1961). Multiple scattering of waves. *Journal of Mathematical Physics*, 2(4), 512-537.
32. Bruning, J., & Lo, Y. (1971). Multiple scattering of EM waves by spheres part I—Multipole expansion and ray-optical solutions. *IEEE Transactions on Antennas and Propagation*, 19(3), 378-390.
33. Wang, H., Zhu, J., Sung, J., Hu, G., Greene, J., Li, Y., Park, S., Kim, W., Lee, M., Yang, Y., & others. (2023). Fourier ptychographic topography. *Optics Express*, 31(7), 11007-11018.
34. Eckert, R., Tian, L., & Waller, L. (2016). Algorithmic self-calibration of illumination angles in Fourier ptychographic microscopy. In *Computational Optical Sensing and Imaging* (pp. CT2D-3). Optica Publishing Group.
35. Balanis, C. A. (2012). *Advanced engineering electromagnetics*. John Wiley & Sons.
36. Pendry, J. B. (1996). Calculating photonic band structure. *Journal of Physics: Condensed Matter*, 8(9), 1085. IOP Publishing.
37. Jin, D., Zhou, R., Yaqoob, Z., & So, P. T. C. (2017). Tomographic phase microscopy: Principles and applications in bioimaging. *JOSA B*, 34(5), B64-B77. Optica Publishing Group.

38. Petersen, K. B., & Pedersen, M. S. (2008). The matrix cookbook. *Technical University of Denmark*, 7(15), 510.
39. Kang, S., Zhou, R., Brelen, M., Mak, H. K., Lin, Y., So, P. T. C., & Yaqoob, Z. (2023). Mapping nanoscale topographic features in thick tissues with speckle diffraction tomography. *Light: Science & Applications*, 12(1), 200. Nature Publishing Group UK London.
40. Kamilov, U. S., Papadopoulos, I. N., Shoreh, M. H., Goy, A., Vonesch, C., Unser, M., & Psaltis, D. (2016). Optical tomographic image reconstruction based on beam propagation and sparse regularization. *IEEE Transactions on Computational Imaging*, 2(1), 59-70.